ARCHIVE OF MECHANICAL ENGINEERING

DOI: 10.24425/ame.2025.153740 2025, Vol. 72, No. 2, pp. 333–358

R. Siva SRINIVAS [1]

Identification of speed-dependent parameters in rotor systems supported on tilting pad journal bearings and active magnetic bearings in the presence of combined misalignment

Received 27 August 2024, **Revised** 6 February 2025, **Accepted** 31 March 2025, **Published online** 5 Mayl 2025

Keywords: misalignment, coupling, active magnetic bearing, full spectrum, tilting pad journal bearing

The present work deals with the identification of speed-dependent misalignment parameters in a multi-disk coupled rotor system supported on Tilting pad journal bearings (TPJB) and Active magnetic bearings (AMB). The stiffness matrix of misaligned coupling is modelled as the sum of static coupling stiffness (SCS) and additive coupling stiffness (ACS) matrices. The presence of parallel and/or angular misalignments gives rise to ACS matrix and its coefficients represent misalignment in/about a given direction. ACS coefficients are time dependent and a suitable mathematical function has been chosen to define the time varying nature of these coefficients. The global equations of motion (EOMs) are assembled and solved in time domain to obtain rotor vibration and AMB current data. This data is processed by full spectrum Fast Fourier Transform, and subsequently input to the identification algorithm. The stiffness and damping of TPJBs, stiffness of AMBs and ACS coefficients that correspond to misalignment are estimated at six different speeds along with speed-invariant disc unbalances, and SCS coefficients. The robustness of algorithm is tested against measurement noise and modelling bias. ACS coefficients have been identified within reasonable error margins. Finally, the method of application of the algorithm to real rotors is presented. The novelty of the work is the development of an inverse problem for the identification of parallel and angular misalignments in real rotors.

✉ R. Siva SRINIVAS, e-mail: siva.srinivas@hal-india.co.in

[1] Aero Engine Research and Design Centre, Hindustan Aeronautics Limited, Bangalore, India

Nomenclature

A	Regressor	k_I	Integral gain
A_g	Leg area	k_D	Derivative gain
b	Regressand	k_{ang}	Angular stiffness of coupling
c	Damping matrix coefficient	k_{rad}	Radial stiffness of coupling
C	Damping matrix	k	Stiffness matrix coefficient
F	Bearing dynamic force matrix	**K**	Stiffness matrix
$\boldsymbol{f}$	Force vector	l_g	Airgap
G	Gyroscopic matrix	**M**	Mass matrix
i	Harmonic index	N	Number of windings
i	Control current	p, q, r, s	Participation factors
i_b	Bias current	$s(t)$	Steering function
i_b	AMB bias current	t	Time
$\mathbf{i}_c$	Complex current $(\text{i}_x + \text{j}\text{i}_y)$	**T**	Transformation matrix
I	Identity matrix	x, y	Translational displacements
j	Imaginary number	**x**	Vector of unknown parameters
k_s	AMB displacement constant	**u**	Complex displacement $(x + \text{j}y)$
k_i	AMB current constant	U	Unbalance
k_P	Proportional gain		

Greek symbols

β	Phase angle	φ	Rotational displacement
δ	Static component	ω	Angular speed
$\Delta\mathbf{K}$	Additive stiffness matrix	μ_0	Free space permeability

Subscripts

ang	Angular	rad	Radial
ACS	Additive coupling stiffness	s	Slave
AMB	Active magnetic bearing	SCS	Static coupling stiffness
b	Bearing	sh	shaft
c	Coupling	TPJB	Tilting pad journal bearing
d	Disc	unb	Unbalance
m	Master		

Superscripts

d	Dynamic	im	Imaginary
fluc	Fluctuating	re	Real
h	Hybrid	rot	Rotating frame of reference

1. Introduction

Active magnetic bearings (AMBs) are mainly used for instability control, condition monitoring of faults, such as the unbalance, cracks, misalignment and rotor vibration attenuation in the presence of faults. This section surveys a few relevant papers from the literature available on misaligned rotors and the applications of AMBs.

In [1], authors provide an extensive review of the uses of AMBs in industrial and laboratory rotor systems. In [2], magnetic bearing constant is estimated using a technique that leverages closed-loop control and air-gap sensor data without needing extra load cells, which commonly introduce signal noise issues. In [3], rotor vibrations are controlled using tilting-pad bearings with electromagnetic actuators to control the motion of pads. In [4], rotor vibrations are reduced using AMBs that use Adaptive Filter based on the Least Mean Square method and an Iterative Search Algorithm. The results show significant vibration reduction, with rotor displacement amplitude decreasing by up to 77%. In [5], axial vibration suppression was achieved in ship propulsion shaft systems, using hybrid AMBs. With active control, significant reduction in base vibration and shaft vibration are achieved. In [6], AMBs are used to improve control and fault diagnosis in spur gear systems. Gear system faults are estimated by model-based identification using full spectrum analysis of vibration and current signals. The utility of AMBs to suppress vibration caused by spur gear transmission errors and misalignment are experimentally shown in [7].

In [8], the influence of unbalance, misalignment, winding defects on the dynamics of spindle supported on AMBs. In [9], an AMB controller is designed that can suppress the multi-harmonic vibration generated due to phenomena such as the fluid interaction, journal bearings, rotor asymmetry, rotor rubs, bearing wear and pulsating torque. In [10], analysis, measurement and balancing of fly wheel which is magnetically suspended on a 3-DOF axial AMB and a 2-DOF radial AMB is performed.

In [11], model-based approach is used to identify faults such as unbalance, sensor misalignment, and AMB misalignment, along with their stiffness parameters in flexible rotor systems. The study introduces a virtual trial misalignment strategy, which simulates misalignment without requiring physical trials. In [12], a model-based approach is developed to estimate inertial parameters of a rigid rotor system experiencing dynamic unbalance, while being supported by AMBs in the presence of noise.

AMB has been used to eliminate the oil-whip instability that occurs at twice the first critical speed using various control laws, such as the μ-synthesis and fuzzy logic control [13–16]. Health monitoring of a cracked rotor system was performed by injecting time-dependent magnetic force using a mid-shaft/outboard support AMBs without the need for extra actuators [17, 18]. *Combination resonances* based on the AMB excitation frequency, shaft rotational speed, and shaft natural frequencies noticed in the spectra are found to be good indicators of breathing crack.

In [19, 20], AMBs are used to improve the operating margin of the axial and centrifugal compressors by allowing to operate in deep surge region using active tip clearance control. In [21], a prototype of TPJB is built with an embedded AMBs that serves the dual function of higher load capacity bearings and actuators. In [22], AMBs are used in conjunction with TPJBs to control the vibration of steam turbine

rotor. In [23], simultaneous identification of faults, such as crack, residual bow, and their interaction is achieved by using multi-harmonic spectral data. The study uses vibrational signal measurements and AMB control current data from a rotor dynamic test bench to identify system parameters that affect the rotor's behavior. In [24], a model-based feed-forward compensation approach of AMBs is used to suppresses base vibration amplitudes in systems such as turbines mounted on ships where external base forces like wave excitations are present. The method proved effective for both harmonic and random base excitations.

In [25], parallel and angular misalignments are induced in a coupled rotor test rig with a six-axis load cell placed under the bearing pedestal to measure the fluctuating forces and moments. The full-spectrum plot of rotor vibration showed integer harmonics from −5 to +5. In [26], a new model of misaligned coupling that had static and additive stiffness components is postulated. In [27], the forces and moments of coupling subjected to misalignment are estimated by identifying the stiffness coefficients from the forced response of rotor using linear regression. In [28], nonlinear dynamic simulations are performed to analyze the system's response under various shock loadings and parametric conditions. Key findings include the identification of critical factors affecting system stability, such as rotor unbalance, the interaction between AMBs and TDB, and the impact of base shock excitation on the rotor's vibrations. In [29, 30], a model is developed to numerically study the effect of number of magnets, air gap and angle on the transient vibration of a misaligned rotor running on two identical AMBs. Both lateral and torsional resonances were found to be excited due to angular misalignment. In [31], the impact of ship maneuvers on the vibrational behavior of rotor system supported by AMBs is studied. The simulation shows that vibration due to maneuvers is more than that due to rotor unbalance. In [32], the authors modelled the static stiffness coefficients of a misaligned coupling, displacement and current stiffness of AMB as speed-dependent parameters and estimated them above the first critical speed of a flexible rotor system.

The author has not come across any work, where ACS coefficients are modelled as speed-dependent parameters or where they have been estimated either numerically or experimentally. In the available literature, misalignment is identified by the presence of multiple harmonics (1×, 2×, . . .) in FFTs or by non-circular rotor orbits. In the present work, misalignment is identified *numerically* in the form of coefficients that are speed-dependent. The scope of this work is the development of mathematical model, generation of response from numerical simulations, development of identification algorithm and estimation of system parameters in the presence of Gaussian white noise in responses. First, the finite element (FE) model of a multi-stage rotor system, whose couplings are subjected to combined misalignment is developed. In the presence of misalignment, the stiffness matrix of coupling is modelled as the sum of static and fluctuating/ (or additive) components. The *weight dominance* criterion, which is applicable to heavy rotors sets is applied to derive the fluctuating forces and moments of coupling. Since the rotor is sup-

ported on TPJBs and AMBs, whose parameters are speed-dependent, for a given amount of misalignment, the forces and moments acting on coupling change with speed [32] with the result that ACS coefficients too would become speed-dependent, while the SCS coefficients would remain constant. A Simulink model is built from the global EOMs of the coupled rotor system. An identification algorithm based on multi-variate linear least-squares problem is developed from frequency domain form of condensed EOMs. The inputs to the algorithm are the real and imaginary parts of rotor vibration and AMB current obtained from full spectrum. The TPJB, AMB and ACS parameters at six different speeds are identified from the inverse problem. To account for modeling uncertainties, measurement noise present in real world data acquisition, a random noise is introduced in the system parameters and vibration responses. The estimates obtained are fairly close to the assumed parameters, demonstrating the robustness of the identification algorithm. The method of application of the proposed algorithm is discussed finally.

2. Problem definition

2.1. Assumptions

1. Torsional vibrations exist in coupled rotor systems due to the presence of flexible couplings. Their effect on the dynamics of rotor system is not considered in the present study.
2. To account for the multi harmonic nature of misalignment force, a suitable mathematical function has been assumed in simulation.

2.2. Mathematical model

This section deals with FE analysis of a multi-stage rotor system connected by intermediate couplings and supported on TPJBs and AMBs. The development of mathematical model of coupling in the presence of combined (parallel and angular) misalignment is discussed.

2.3. Shaft and rigid disc

Timoshenko beam finite elements having two-nodes per element have been used to model the rotor system. The elemental shaft matrices used for mathematical modeling in this work are given in [33]. These elemental shaft matrices are developed in *complex* domain and represent the motion of rotor in two transverse planes. As they are developed in complex domain, the size of the elemental matrices reduces by a factor 2, which results in conciseness and computational efficiency. $\mathbf{M}$, $\mathbf{K}$ matrices are 4×4 symmetric matrices with real coefficients. $\mathbf{G}$ is a 4×4 skew-symmetric matrix with real coefficients. Likewise, the $\mathbf{M}$ and $\mathbf{G}$ matrices of rigid discs of size 2×2 given in [34] are used in the present work. Since the disc is considered rigid, there is no corresponding $\mathbf{K}$ matrix.

The complex displacement vector obtained from the generalized coordinates of beam element is given in [33]

$$\mathbf{u}^e = \mathbf{u}_{xz} + \mathrm{j}\mathbf{u}_{yz} = \left\{x_1 \quad \varphi_{y_1} \quad x_2 \quad \varphi_{y_2}\right\}^{\mathrm{T}} + \mathrm{j}\left\{y_1 \quad \varphi_{x_1} \quad y_2 \quad \varphi_{x_2}\right\}^{\mathrm{T}}. \tag{1}$$

2.4. Tilting pad journal bearings

At a *given* speed ω the complex bearing dynamic forces due to stiffness and damping are given in [34].

$$F(\omega) = -\begin{bmatrix} k_{xx}(\omega) & 0 \\ 0 & k_{yy}(\omega) \end{bmatrix}\begin{Bmatrix} x \\ y \end{Bmatrix} - \begin{bmatrix} c_{xx}(\omega) & 0 \\ 0 & c_{yy}(\omega) \end{bmatrix}\begin{Bmatrix} \dot{x} \\ \dot{y} \end{Bmatrix} \tag{2}$$

The translational displacements are rewritten in terms of complex displacements as $x = (u + \bar{u})/2$, $y = -\mathrm{j}(u - \bar{u})/2$, where $u = x + \mathrm{j}y$, $\bar{u} = x - \mathrm{j}y$. Eq. (2) then takes the following complex form

$$\begin{aligned} F(\omega) = &-0.5\begin{bmatrix} k_{xx}(\omega) & 0 \\ 0 & k_{yy}(\omega) \end{bmatrix}\begin{Bmatrix} u + \bar{u} \\ -\mathrm{j}(u - \bar{u}) \end{Bmatrix} \\ &-0.5\begin{bmatrix} c_{xx}(\omega) & 0 \\ 0 & c_{yy}(\omega) \end{bmatrix}\begin{Bmatrix} \dot{u} + \dot{\bar{u}} \\ -\mathrm{j}(\dot{u} - \dot{\bar{u}}) \end{Bmatrix}, \end{aligned} \tag{3}$$

$k_{xx}(\omega)$, $k_{yy}(\omega)$, $c_{xx}(\omega)$, $c_{yy}(\omega)$ are the direct stiffness and damping coefficients of TPJB in x and y directions. For the *lbp* configuration (Fig. 1a), if the number of pads is even, the load is shared equally by the two bottom pads ($k_{xx}(\omega) = k_{yy}(\omega)$) and if the number of pads is odd, the load is shared unequally by the two bottom pads ($k_{xx}(\omega) \neq k_{yy}(\omega)$). For the *lop* configuration, Fig. 1b, the majority of the load is felt by the bottommost pad and $k_{xx}(\omega) \neq k_{yy}(\omega)$ [34]. In contrast, in plain journal bearings, in certain idealized cases, such as when the bearing operates at very low loads, low speeds, or under perfectly symmetric conditions, the stiffness coefficients may approach equality.

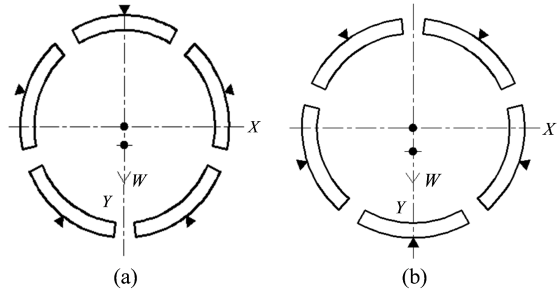

Fig. 1. TPJB configurations: (a) load between pivot (*lbp*), (b) load on pivot (*lop*)

2.5. Active magnetic bearings

The control force exerted by AMB in differential control mode in a given direction are given in [35, 36]

$$f_{\text{AMB}} = \left\{c_1(i_b + i_c)^2/(l_g + u_{\text{AMB}})^2\right\} - \left\{c_1(i_b - i_c)^2/(l_g - u_{\text{AMB}})^2\right\}, \quad (4)$$

where $c_1 = k\mu_0 N^2 A_g$. For thrust AMBs the constant k is 0.25 and for radial AMBs k is 1. u_{AMB} is the displacement of the AMB rotor in the control plane, l_g is the airgap; i_b is the bias current; μ_0 is the free space permeability $(4\pi \times 10^{-7})$; N is the number of windings; A_g is the leg area. Over the normal operating range of AMB $u_{\text{AMB}} \ll l_g$ with the result that the nonlinear forces are negligible.

The control current in AMB coils controlled by proportional-integral-derivative (PID) law is given by

$$\mathbf{i}_c = k_P \mathbf{u}_{\text{AMB}} + k_I \int \mathbf{u}_{\text{AMB}}\, \mathrm{d}t + k_D \dot{\mathbf{u}}_{\text{AMB}}\,, \quad (5)$$

where k_P, k_I and k_D are the proportional, integral and derivative gains, respectively.

The AMB force vector in complex form can be written as

$$\boldsymbol{f}_{\text{AMB}} = -k_s \mathbf{u}_{\text{AMB}} + k_i \mathbf{i}_c\,, \quad (6)$$

where AMB displacement constant $k_s = 4c_1 i_b^2/l_g^3$, AMB current constant $k_i = 4c_1 i_b/l_g^2$; $\mathbf{u}_{\text{AMB}}$ is the displacement of the AMB rotor in the control plane.

Due to the speed-dependent nature of unbalance and misalignment forces, there will be a shift in the equilibrium position of rotor within the AMB clearance about the geometric center line with the change in rotor speed, as shown in Fig. 2a. Fig. 2b shows a nonlinear nature of *magnetic force versus operating point* curve. Each point on the curve depends on the force caused due to external disturbances, which in turn varies with the rotor speed. As the rotor's operating speed changes the operating point shifts and there is a corresponding change in slope of the curve (k_s). This leads to a change in the AMB current required, which in turn causes a shift in the slope of the curve (k_i), as shown in Fig. 2c.

Thus, stiffness constants of AMB, which are otherwise not varying, change due to the disturbances that vary with operating speed. Thus, in the presence of external forces, such as unbalance and misalignment, it would be practical to rewrite the AMB force as

$$\boldsymbol{f}_{\text{AMB}}(\omega) = -k_s(\omega)\mathbf{u}_{\text{AMB}} + k_i(\omega)\mathbf{i}_c\,. \quad (7)$$

The speed-dependent nature of AMB force is the result of vibratory motion of rotor due to speed-dependent excitation forces, such as unbalance and misalignment.

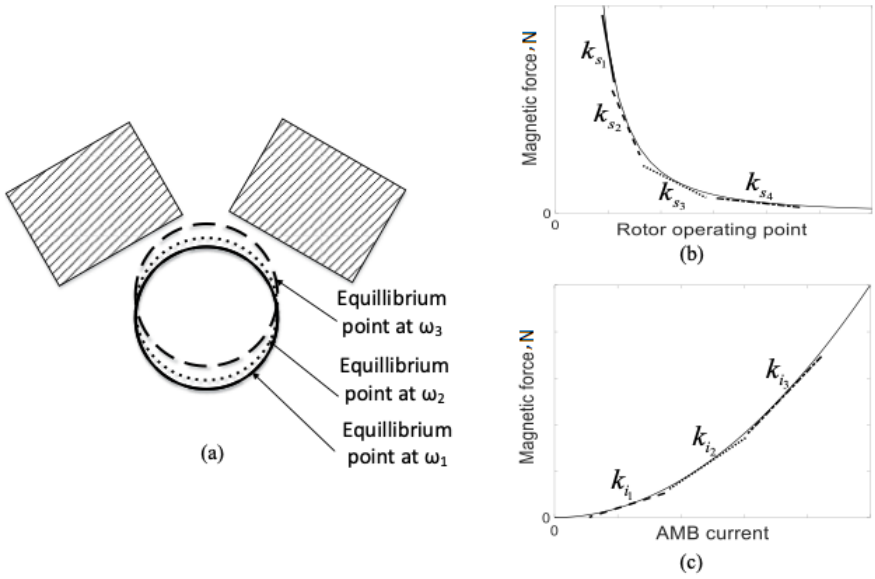

Fig. 2. (a) Operating point of rotor at various speeds inside AMB clearance (hatched lines indicate coil turnings); (b) AMB force versus operating point; (c) AMB force versus AMB current

2.6. Mathematical model of misaligned coupling

In the presence of misalignment (Fig. 3a), the stiffness of coupling is written as the sum of static stiffness $\mathbf{K}_c^{\text{mean}}$, which produces static coupling force, $\mathbf{f}_{\text{SCS}}$ and time-varying additive stiffness $\Delta\mathbf{K}(t)_c^{\text{fluc}}$, which produces a fluctuating component of force, $\mathbf{f}_{\text{ACS}}$ [26]. $\mathbf{f}_{\text{SCS}}$ is speed-independent and $\mathbf{f}_{\text{ACS}}$ is speed-dependent parameter and both the forces are in rotating frame of reference (Fig. 3c).

$$\begin{aligned}\mathbf{f}_{\text{coupling}} &= \left[\mathbf{K}_c^{\text{mean}} + \Delta\mathbf{K}(t)_c^{\text{fluc}}\right]\left\{\mathbf{u}_{0c}^{\text{rot}} + \mathbf{u}_c^{\text{rot}}(t)\right\} \\ &= \underbrace{\mathbf{K}_c^{\text{mean}}\mathbf{u}_c^{\text{rot}}}_{\mathbf{f}_{\text{SCS}}} + \underbrace{\Delta\mathbf{K}(t)_c^{\text{fluc}}\mathbf{u}_{0c}^{\text{rot}} + \Delta\mathbf{K}(t)_c^{\text{fluc}}\mathbf{u}_c^{\text{rot}}}_{\mathbf{f}_{\text{ACS}}(\omega)}\end{aligned} \tag{8}$$

with

$$\mathbf{u}_{0c}^{\text{rot}} = \left\{\delta\xi_c \quad \delta\eta_c \quad \delta\varphi_{\eta_c} \quad \delta\varphi_{\xi_c} \quad \delta\xi_{c+1} \quad \delta\eta_{c+1} \quad \delta\varphi_{\eta_{c+1}} \quad \delta\varphi_{\xi_{c+1}}\right\}^{\text{T}}, \tag{9}$$

$$\mathbf{u}_c^{\text{rot}} = \left\{\xi_c \quad \eta_c \quad \varphi_{\eta_c} \quad \varphi_{\xi_c} \quad \xi_{c+1} \quad \eta_{c+1} \quad \varphi_{\eta_{c+1}} \quad \varphi_{\xi_{c+1}}\right\}^{\text{T}}, \tag{10}$$

where Eqs. (9), (10) denote the coupling's static and vibratory displacements in rotating frame of reference (Fig. 3c).

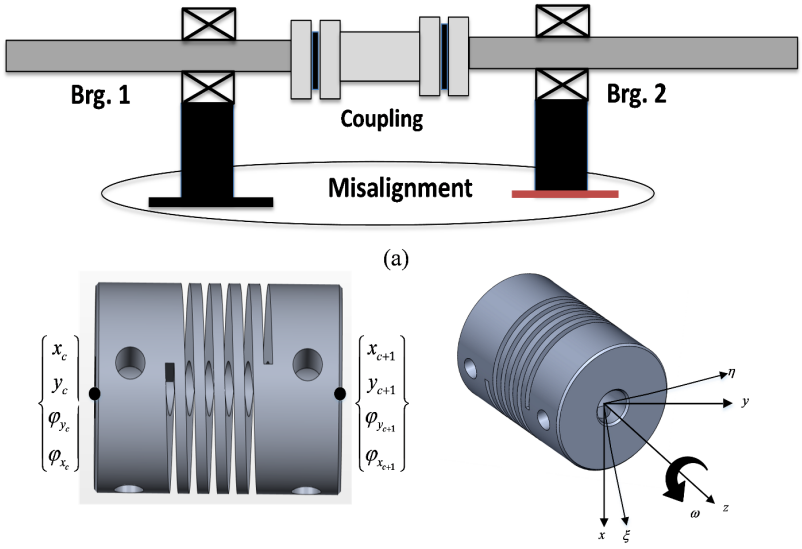

Fig. 3. (a) Schematic of misaligned coupling, (b) Generalized coordinates of coupling, (c) Stationary and rotational frames of reference

The static and additive stiffness matrices of coupling stiffness in Eq. (8) are denoted by Eqs. (11), (12)

$$\mathbf{K}_c^{\text{mean}} = \begin{bmatrix} k_{xx} & k_{xy} & 0 & 0 & -k_{xx} & -k_{xy} & 0 & 0 \\ k_{yx} & k_{yy} & 0 & 0 & -k_{yx} & -k_{yy} & 0 & 0 \\ 0 & 0 & k_{\varphi_y\varphi_y} & 0 & 0 & 0 & -k_{\varphi_y\varphi_y} & 0 \\ 0 & 0 & 0 & k_{\varphi_x\varphi_x} & 0 & 0 & 0 & -k_{\varphi_x\varphi_x} \\ -k_{xx} & -k_{xy} & 0 & 0 & k_{xx} & k_{xy} & 0 & 0 \\ -k_{yx} & -k_{yy} & 0 & 0 & k_{yx} & k_{yy} & 0 & 0 \\ 0 & 0 & -k_{\varphi_y\varphi_y} & 0 & 0 & 0 & k_{\varphi_y\varphi_y} & 0 \\ 0 & 0 & 0 & -k_{\varphi_x\varphi_x} & 0 & 0 & 0 & k_{\varphi_x\varphi_x} \end{bmatrix}, \tag{11}$$

$$\Delta\mathbf{K}_c^{\text{rot}} = \begin{bmatrix} \Delta k_{\xi\xi} & 0 & 0 & 0 & -\Delta k_{\xi\xi} & 0 & 0 & 0 \\ 0 & \Delta k_{\eta\eta} & 0 & 0 & 0 & -\Delta k_{\eta\eta} & 0 & 0 \\ 0 & 0 & \Delta k_{\varphi_\eta\varphi_\eta} & 0 & 0 & 0 & -\Delta k_{\varphi_\eta\varphi_\eta} & 0 \\ 0 & 0 & 0 & \Delta k_{\varphi_\xi\varphi_\xi} & 0 & 0 & 0 & -\Delta k_{\varphi_\xi\varphi_\xi} \\ -\Delta k_{\xi\xi} & 0 & 0 & 0 & \Delta k_{\xi\xi} & 0 & 0 & 0 \\ 0 & -\Delta k_{\eta\eta} & 0 & 0 & 0 & \Delta k_{\eta\eta} & 0 & 0 \\ 0 & 0 & -\Delta k_{\varphi_\eta\varphi_\eta} & 0 & 0 & 0 & \Delta k_{\varphi_\eta\varphi_\eta} & 0 \\ 0 & 0 & 0 & -\Delta k_{\varphi_\xi\varphi_\xi} & 0 & 0 & 0 & \Delta k_{\varphi_\xi\varphi_\xi} \end{bmatrix}. \tag{12}$$

The static part of coupling stiffness is unchanging and exists with or without misalignment. The additive stiffness part exists only when misalignment is present. In this regard its behavior is similar to rotors with breathing crack studied in [23]. The number of amplitude of harmonics depend on the severity of misalignment. The coefficients of ACS matrix given by Eq. (12) correspond to misalignment in/about the directions denoted by their subscripts. For example, $\Delta k_{\xi\xi}$ denotes misalignment *in* ξ direction in Fig. 3c. Likewise, $\Delta k_{\varphi_\xi\varphi_\xi}$ denotes misalignment *about* ξ direction.

2.6.1. Force due to coupling's static stiffness in stationary frame

For the sake of simplicity, the cross-coupling stiffness coefficients in Eq. (11) are ignored and k_{xx},k_{yy} are assumed to be equal to k_{rad}, the stiffness of coupling in radial direction. Likewise, the coefficients $k_{\varphi_y\varphi_y}$, $k_{\varphi_x\varphi_x}$ are assumed to be equal to k_{ang}, the stiffness of coupling in angular direction. The final complex form of static stiffness force of coupling $\mathbf{f}_{\text{ACS}}$ after performing coordinate transformation from rotating to stationary frame of reference (Fig. 3c) is given by

$$\mathbf{f}_{\text{SCS}} = \begin{bmatrix} k_{\text{rad}} & 0 & -k_{\text{rad}} & 0 \\ 0 & k_{\text{ang}} & 0 & -k_{\text{ang}} \\ -k_{\text{rad}} & 0 & k_{\text{rad}} & 0 \\ 0 & -k_{\text{ang}} & 0 & k_{\text{ang}} \end{bmatrix} \begin{Bmatrix} u_c \\ \varphi_c \\ u_{c+1} \\ \varphi_{c+1} \end{Bmatrix}, \tag{13}$$

where $u_c = x_c + \mathrm{j}y_c$, $u_{c+1} = x_{c+1} + \mathrm{j}y_{c+1}\varphi_c = \varphi_{y_c} + \mathrm{j}\varphi_{x_c}$, $\varphi_{c+1} = \varphi_{y_{c+1}} + \mathrm{j}\varphi_{x_{c+1}}$ in Eq. (13) are the complex displacements at coupling nodes in stationary frame of reference.

2.6.2. Force due to additive stiffness of coupling in stationary frame

The additive coupling stiffness part of Eq. (8) contains both static displacements and vibratory displacements at coupling nodes. If vibratory part of displacement is also considered, the resulting equation would contain terms which are the product of multi-harmonic terms of steering function $\Delta\mathbf{K}_c^{\text{rot}}(t)$ and $\mathbf{u}_c^{\text{rot}}$, i.e., translational and rotational displacements, which are also harmonic inc nature. This product results in a more complex formulation of the coupling stiffness. To simplify without loss of generality, the present mathematical model of coupling is based on the assumption that in heavy multi-stage turbogenerators, the vibratory displacement at coupling nodes is smaller than the corresponding static deflections (*weight dominance*) [38].

$$\mathbf{u}_c(t) \approx \mathbf{u}_{0c}\,. \tag{14}$$

The fluctuating coupling force $\mathbf{f}_{\text{ACS}}$ in the second part of Eq. (8) then becomes

$$\mathbf{f}_{\text{ACS}}^{\text{rot}} = \Delta\mathbf{K}_c^{\text{rot}}(t)\mathbf{u}_{0c}^{\text{rot}}, \tag{15}$$

where $\Delta\mathbf{K}_c^{\text{rot}}(t)$ is the additive stiffness of coupling, which varies in time with rotation angle. Hence, Eq. (15) is written as the product of matrix of constant coefficients $\Delta\mathbf{K}_c^{\text{rot}}$ and an appropriate time waveform $s(t)$, which is called the steering function (Fig. 4).This particular waveform has been chosen since this generates multiple integer harmonics of rotor vibration in frequency domain plot as observed in experimental studies conducted in [25]. This multi-harmonic behavior containing all integer harmonics was not observed with other wave forms (e.g., 50% duty cycle, saw tooth wave form). Hence, 40% duty cycle waveform is found to be suitable for numerical simulation of multi-harmonic nature of misalignment force.

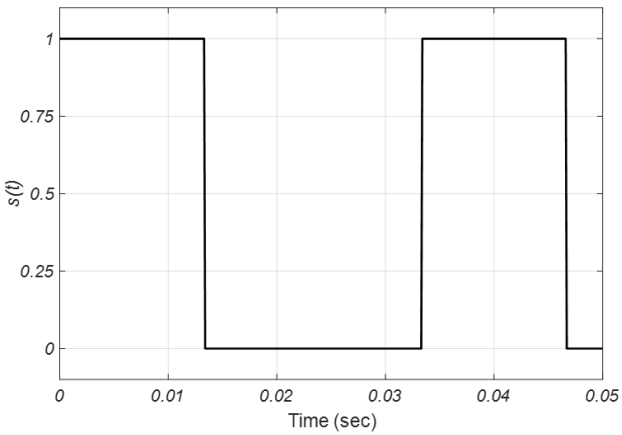

Fig. 4. $s(t)$: rectangular wave with 40% duty cycle

Therefore Eq. (15) can be rewritten as

$$\mathbf{f}_{\text{ACS}}^{\text{rot}} = s(t)\Delta\mathbf{K}_c^{\text{rot}}\mathbf{u}_{0c}^{\text{rot}}. \tag{16}$$

The Fourier expansion of the time series $s(t)$ shown in Fig. 4 is given by following equation:

$$\begin{aligned} s(t) = {} & 0.5 + 0.6055\cos(\omega t) + 0.1871\cos(2\omega t) - 0.1247\cos(3\omega t) \\ & - 0.1514\cos(4\omega t) + 0.1009\cos(6\omega t) + 0.0535\cos(7\omega t) \\ & - 0.0468\cos(8\omega t) - 0.0673\cos(9\omega t) + 0.055\cos(11\omega t) \\ & + 0.0312\cos(12\omega t) - 0.0288\cos(13\omega t) - 0.0432\cos(14\omega t) \\ & + 0.0378\cos(16\omega t) + 0.022\cos(17\omega t) + \ldots \end{aligned} \tag{17}$$

Upon substituting Eq. (9), (12), (17) into Eq. (16), the final complex form of $\mathbf{f}_{\mathrm{ACS}}$ in stationary frame of reference is given by

$$\mathbf{f}_{\mathrm{ACS}}(\omega) = 0.5 \begin{Bmatrix} (\delta x_c - \delta x_{c+1}) \left(\Delta k^{\omega}_{\xi\xi} \sum_{i=-n}^{i+n} p_i e^{\mathrm{j}i\omega t} + \Delta k^{\omega}_{\eta\eta} \sum_{i=-n}^{i+n} q_i e^{\mathrm{j}i\omega t} \right) \\ (\delta\varphi_{y_c} - \delta\varphi_{y_{c+1}}) \left(\Delta k^{\omega}_{\varphi_\xi\varphi_\xi} \sum_{i=-n}^{i+n} r_i e^{\mathrm{j}i\omega t} + \Delta k^{\omega}_{\varphi_\eta\varphi_\eta} \sum_{i=-n}^{i+n} s_i e^{\mathrm{j}i\omega t} \right) \\ (\delta x_{c+1} - \delta x_c) \left(\Delta k^{\omega}_{\xi\xi} \sum_{i=-n}^{i+n} p_i e^{\mathrm{j}i\omega t} + \Delta k^{\omega}_{\eta\eta} \sum_{i=-n}^{i+n} q_i e^{\mathrm{j}i\omega t} \right) \\ (\delta\varphi_{y_{c+1}} - \delta\varphi_{y_c}) \left(\Delta k^{\omega}_{\varphi_\xi\varphi_\xi} \sum_{i=-n}^{i+n} r_i e^{\mathrm{j}i\omega t} + \Delta k^{\omega}_{\varphi_\eta\varphi_\eta} \sum_{i=-n}^{i+n} s_i e^{\mathrm{j}i\omega t} \right) \end{Bmatrix}. \quad (18)$$

The interpretation of Eq. (18) is as follows: a given amount of parallel and/or angular misalignment generates speed dependent ACS coefficients and speed dependent misalignment forces. Hence ω is attached as superscript to various Δk coefficients. δx_c, δx_{c+1}, $\delta\varphi_{y_c}$, $\delta\varphi_{y_{c+1}}$, which are the static deflections at coupling nodes, can obtained from the catenary curve or static deflection curve [38]. p_i, q_i, r_i, and s_i are the participation factors of various harmonics from $i = -n$ to $i = +n$ arising due to misalignment.

An important point is to be highlighted as a concluding remark for this section. The steering function shown in Fig. 4 and given by Eq. (17) is chosen to mimic the response of real misaligned rotors. In real rotors, the actual steering function that governs misalignment can be reconstructed from the amplitude of the participation factors of various harmonics. This was performed in [37] for the case of cracked Jeffcott rotor.

2.7. Force due to unbalance

The force due to the unbalance eccentricities at various disc locations is

$$\mathbf{f}_{\mathrm{unb}} = m_d e \omega^2 e^{\mathrm{j}\omega t} e^{\mathrm{j}\beta}, \quad (19)$$

where e is the disc unbalance eccentricity located at the phase angle β.

2.8. Global EOM

Eq. (20) is the complex form of global EOMs of the coupled rotor system, as

$$\begin{aligned} &(\mathbf{M}_{\mathrm{sh}} + \mathbf{M}_d)\,\ddot{\mathbf{u}} + [\mathbf{C}_b(\omega) + \mathbf{C}_c + \mathbf{C}_{sh} - \mathrm{j}\omega(\mathbf{G}_{sh} + \mathbf{G}_d)]\,\dot{\mathbf{u}} \\ &\quad + (\mathbf{K}_b(\omega) + \mathbf{K}_{\mathrm{SCS}} + \mathbf{K}_{\mathrm{sh}})\,\mathbf{u} = \mathbf{f}_{\mathrm{unb}} + \mathbf{f}_{\mathrm{AMB}}(\omega) - \mathbf{f}_{\mathrm{ACS}}(\omega). \end{aligned} \quad (20)$$

The subscripts sh, d, b, c refers to shaft, disc, bearing and coupling matrices, respectively. The assumed solution to Eq. (20) is of following form

$$\mathbf{u}_m = \sum_{i=-\infty}^{i=+\infty} \bar{\mathbf{u}}_m e^{\mathrm{j}i\omega t}. \tag{21}$$

Since AMB is a support bearing it experiences force which has the same multi-harmonic nature as rotor displacement. In such case, the complex current vector $\mathbf{i}_c$ of AMB present in Eq.(6) assumes the following form

$$\mathbf{i}_c = \sum_{i=-\infty}^{i=+\infty} \bar{\mathbf{i}}_c e^{\mathrm{j}i\omega t}. \tag{22}$$

The force vectors, on the right side of Eq. (20) are given by

$$\bar{\mathbf{f}}_{\mathrm{unb}} = \bar{\mathbf{f}}_{\mathrm{unb}} e^{i\omega t}; \quad \bar{\mathbf{f}}_{\mathrm{AMB}}(\omega) = \bar{\mathbf{f}}_{\mathrm{AMB}}(\omega) e^{\mathrm{j}i\omega t}; \quad \bar{\mathbf{f}}_{\mathrm{ACS}} = \bar{\mathbf{f}}_{\mathrm{ACS}}(\omega) e^{\mathrm{j}i\omega t}$$

Substituting Eq. (21) and (22) into Eq. (20) converts global EOM in time domain to frequency domain which is given by:

$$\left(-\mathbf{M}(i\omega)^2 + \mathrm{j}(i\omega)\left(\mathbf{C} - \mathrm{j}\omega\mathbf{G}\right) + \mathbf{K}\right)\bar{\mathbf{u}} = \bar{\mathbf{f}}_{\mathrm{unb}} + \bar{\mathbf{f}}_{\mathrm{AMB}}(\omega) - \bar{\mathbf{f}}_{\mathrm{ACS}}(\omega) \tag{23}$$

with

$$\mathbf{M} = \mathbf{M}_{\mathrm{sh}} + \mathbf{M}_d; \quad \mathbf{C} = \mathbf{C}_b(\omega) + \mathbf{C}_c + \mathbf{C}_{\mathrm{sh}}; \quad \mathbf{G} = \mathbf{G}_{\mathrm{sh}} + \mathbf{G}_d; \quad \mathbf{K} = \mathbf{K}_b(\omega) + \mathbf{K}_{\mathrm{SCS}} + \mathbf{K}_{\mathrm{sh}}.$$

The development of global EOM of coupled rotor system in time domain and conversion to frequency domain is discussed in this section. Solving Eq. (23) requires obtaining responses at all nodal locations which is not possible in experiments. So, we adopt a condensation procedure to reduce the number of measurement locations, which is discussed in the next section.

2.9. Condensation of Global EOM

The nodes where the external forces act on the rotor system are usually chosen as master DOFs. The rest of the DOFs are grouped as slave DOFs. In the present case, the master DOFs correspond to the nodal locations of *all identifiable parameters*. Eq. (24) lists the master nodes which include the translational DOFs at the nodal locations of TJBs, discs, coupling, AMBs and rotational DOFs at coupling nodes

$$\begin{aligned}\mathbf{u}_m = \Big\{ & u_{\mathrm{AMB}_1} \quad u_{d_1} \quad u_{d_2} \quad u_{\mathrm{TPJB}_1} \quad u_{c_1} \quad \varphi_{c_1} \quad u_{c_2} \quad \varphi_{c_2} \quad u_{\mathrm{TPJB}_2} \\ & u_{d_3} \quad u_{d_4} \quad u_{\mathrm{AMB}_2} \quad \ldots \quad u_{\mathrm{AMB}_{n-1}} \quad u_{d_{n-1}} \quad \ldots \quad u_{c_{n-1}} \\ & \varphi_{c_{n-1}} \quad u_{c_n} \quad \varphi_{c_n} \quad \ldots \quad u_{\mathrm{TPJB}_n} \quad u_{d_n} \quad u_{\mathrm{AMB}_n} \Big\}^{\mathrm{T}}.\end{aligned} \tag{24}$$

The master DOFs can be linked to the total DOFs as shown in Eq. (25) (ref. [33])

$$\mathbf{u} = \begin{Bmatrix} \mathbf{u}_m \\ \mathbf{u}_s \end{Bmatrix} = \mathbf{T}^d \mathbf{u}_m \,. \tag{25}$$

The linking matrix $\mathbf{T}^d$ in Eq. (25) is called the transformation matrix and is given by

$$\mathbf{T}^d = \begin{Bmatrix} \mathbf{I} \\ -[\mathbf{K}_{ss} - \omega_0^2 \mathbf{M}_{ss} - \mathrm{j}\omega_0^2 \mathbf{G}_{ss}]^{-1} [\mathbf{K}_{sm} - \omega_0^2 \mathbf{M}_{sm} - \mathrm{j}\mathbf{G}_{sm}] \end{Bmatrix}. \tag{26}$$

In Eq. (26), ω_0 is the mean speed at which dynamic condensation is performed. Eq. (23) rewritten in terms of reduced coordinates is given by

$$\left(-\mathbf{M}^d (i\omega)^2 + \mathrm{j}(i\omega)\left(\mathbf{C}^d - \mathrm{j}\omega \mathbf{G}^d\right) + \mathbf{K}^d\right) \bar{\mathbf{u}}_m = \bar{\mathbf{f}}^d_{\mathrm{unb}} + \bar{\mathbf{f}}^d_{\mathrm{AMB}}(\omega) - \bar{\mathbf{f}}^d_{\mathrm{ACS}}(\omega) \tag{27}$$

with

$$\mathbf{M}^d = \left(\mathbf{T}^d\right)^T \mathbf{M}\mathbf{T}^d, \quad \mathbf{K}^d = \left(\mathbf{T}^d\right)^T \mathbf{K}\mathbf{T}^d, \quad \mathbf{C}^d = \left(\mathbf{T}^d\right)^T \mathbf{C}\mathbf{T}^d, \quad \mathbf{G}^d = \left(\mathbf{T}^d\right)^T \mathbf{G}\mathbf{T}^d,$$

$$\mathbf{f}^d_{\mathrm{unb}} = \left(\mathbf{T}^d\right)^T \mathbf{f}_{\mathrm{unb}}, \quad \mathbf{f}^d_{\mathrm{AMB}}(\omega) = \left(\mathbf{T}^d\right)^T \mathbf{f}_{\mathrm{AMB}}(\omega), \quad \mathbf{f}^d_{\mathrm{ACS}}(\omega) = \left(\mathbf{T}^d\right)^T \mathbf{f}_{\mathrm{ACS}}(\omega).$$

The superscript d that appears in all the terms in Eq. (27) refers to the dynamically reduced form of matrices and vectors. Of all the master DOFs given by Eq. (24), the rotational DOFs of coupling $\varphi_{c_1}, \varphi_{c_2}, \ldots, \varphi_{c_n}$, which are linked to k_{ang}, $\Delta k_{R\xi}$ and $\Delta k_{R\eta}$ are difficult to measure experimentally. Hence, another stage of reduction called *hybrid* condensation [27] is performed by grouping these DOFs as slave DOFs. The *hybrid* master DOF are linked to master DOF as shown in the following equation:

$$\mathbf{u}_d = \begin{Bmatrix} \mathbf{u}_h \\ \mathbf{u}_{hs} \end{Bmatrix} = \mathbf{T}^h \mathbf{u}_h \,. \tag{28}$$

The transformation matrix $\mathbf{T}^h$ in Eq. (28) used to perform the hybrid condensation is given by

$$\mathbf{T}^h = \begin{Bmatrix} \mathbf{I} \\ -[\mathbf{K}^d_{ss} - \omega_0^2 \mathbf{M}^d_{ss} - \mathrm{j}\omega_0^2 \mathbf{G}^d_{ss}]^{-1} [\mathbf{K}^d_{sm} - \omega_0^2 \mathbf{M}^d_{sm} - \mathrm{j}\mathbf{G}^d_{sm}] \end{Bmatrix}. \tag{29}$$

The complex displacement vector $\mathbf{u}_h$ in Eq. (28) is given by

$$\mathbf{u}_h = \Big\{ u_{d_1} \;\; u_{d_2} \;\; u_{\mathrm{TPJB}_1} \;\; u_{c_1} \;\; u_{c_2} \;\; u_{\mathrm{TPJB}_2} \;\; u_{d_3} \;\; u_{d_4} \;\; u_{\mathrm{AMB}_2} \;\; \ldots$$
$$u_{\mathrm{AMB}_{n-1}} \;\; u_{d_{n-1}} \;\; \ldots \;\; u_{c_{n-1}} \;\; u_{c_n} \;\; \ldots \;\; u_{\mathrm{TPJB}_n} \;\; u_{d_n} \;\; u_{\mathrm{AMB}_n} \Big\}^{\mathrm{T}}. \tag{30}$$

It can be seen that the two-fold condensation has achieved the reduction of DOFs that needs to be measured. The hybrid master DOFs shown in Eq. (30) consist only of translational DOFs which can be measured readily.

The final EOM in terms of hybrid DOF in frequency domain is given by

$$\left(-\mathbf{M}^h(i\omega)^2 + \mathrm{j}(i\omega)\left(\mathbf{C}^h - \mathrm{j}\omega\mathbf{G}^h\right) + \mathbf{K}^h\right)\bar{\mathbf{u}}_h = \mathbf{f}^h_{\mathrm{unb}} + \mathbf{f}^h_{\mathrm{AMB}}(\omega) - \mathbf{f}^h_{\mathrm{ACS}}(\omega), \quad (31)$$

where

$$\mathbf{M}^h = \left(\mathbf{T}^h\right)^T\mathbf{M}^d\mathbf{T}^h, \quad \mathbf{K}^h = \left(\mathbf{T}^h\right)^T\mathbf{K}^d\mathbf{T}^h, \quad \mathbf{C}^h = \left(\mathbf{T}^h\right)^T\mathbf{C}^d\mathbf{T}^h, \quad \mathbf{G}^h = \left(\mathbf{T}^h\right)^T\mathbf{G}^d\mathbf{T}^h,$$

$$\mathbf{f}^h_{\mathrm{unb}} = \left(\mathbf{T}^h\right)^T\mathbf{f}^d_{\mathrm{unb}}, \quad \mathbf{f}^h_{\mathrm{AMB}}(\omega) = \left(\mathbf{T}^h\right)^T\mathbf{f}^d_{\mathrm{AMB}}(\omega), \quad \mathbf{f}^h_{\mathrm{ACS}}(\omega) = \left(\mathbf{T}^h\right)^T\mathbf{f}^d_{\mathrm{ACS}}(\omega).$$

The superscript $h$that appears in all the terms in Eq. (31) refers to matrices and vectors in *hybrid* reduction form.

In this section the global EOM is rewritten in terms of translational DOFs which can be readily measured on test rotors. The development of identification algorithm is explained in the next section.

2.10. Development of inverse problem for parameter estimation

Eq. (31) can be rearranged by relocating all the unknown parameters (disc unbalance, coupling static and additive stiffness coefficients, TPJB stiffness and damping, AMB constants) to the right side in the following form

$$\begin{aligned}\left(-\mathbf{M}^h(i\omega)^2 + \mathrm{j}(i\omega)\left(\mathbf{C}^h_{sh+c} - \mathrm{j}\omega\mathbf{G}^h\right) + \mathbf{K}^h_{\mathrm{sh}}\right)\bar{\mathbf{u}}_h \\ = \bar{\mathbf{f}}^h_{\mathrm{unb}} - \bar{\mathbf{f}}^h_{\mathrm{SCS}} + \bar{\mathbf{f}}^h_{\mathrm{AMB}}(\omega) - \mathbf{f}^h_{\mathrm{ACS}}(\omega) - \bar{\mathbf{f}}^h_{\mathrm{brgk}}(\omega) - \bar{\mathbf{f}}^h_{\mathrm{brgc}}(\omega). \quad (32)\end{aligned}$$

At a given speed ω, Eq. (32) can be partitioned as follows

$$\left\{\mathbf{A}_{\mathrm{unb}} \quad \mathbf{A}_{\mathrm{SCS}} \quad \mathbf{A}_{\mathrm{ACS}}(\omega) \quad \mathbf{A}_{\mathrm{TPJB}}(\omega) \quad \mathbf{A}_{\mathrm{AMB}}(\omega)\right\}\begin{Bmatrix}\mathbf{x}_{\mathrm{unb}}\\ \mathbf{x}_{\mathrm{SCS}}\\ \mathbf{x}_{\mathrm{ACS}}(\omega)\\ \mathbf{x}_{\mathrm{TPJB}}(\omega)\\ \mathbf{x}_{\mathrm{AMB}}(\omega)\end{Bmatrix} = \mathbf{b}(\omega), \quad (33)$$

where:

$$\mathbf{x}_{\mathrm{unb}} = \left\{U_1^{\mathrm{re}} \quad U_1^{\mathrm{im}} \quad U_2^{\mathrm{re}} \quad U_2^{\mathrm{im}} \quad U_3^{\mathrm{re}} \quad U_3^{\mathrm{im}} \quad U_4^{\mathrm{re}} \quad U_4^{\mathrm{im}}\right\}^{\mathrm{T}},$$

$$\mathbf{x}_{\mathrm{SCS}} = \left\{k_{\mathrm{rad}} \quad k_{\mathrm{ang}}\right\}^{\mathrm{T}},$$

$$\mathbf{x}_{\mathrm{TPJB}}(\omega) = \left\{k_{\mathrm{TPJB}_1}(\omega) \quad k_{\mathrm{TPJB}_2}(\omega) \quad c_{\mathrm{TPJB}_1}(\omega) \quad c_{\mathrm{TPJB}_2}(\omega)\right\}^{\mathrm{T}},$$

$$\mathbf{x}_{\mathrm{AMB}}(\omega) = \left\{k_s(\omega) \quad k_i(\omega)\right\}^{\mathrm{T}},$$

$$\mathbf{x}_{\mathrm{ACS}}(\omega) = \left\{\Delta k_{\eta\eta}(\omega) \quad \Delta k_{\eta\eta}(\omega) \quad \Delta k_{\varphi_\eta\varphi_\eta}(\omega) \quad \Delta k_{\varphi_\xi\varphi_\xi}(\omega)\right\}^{\mathrm{T}}.$$

The vector of unknown parameters $\mathbf{x}$ in Eq. (33) consists of speed-dependent and speed-independent parameters. For each speed of interest ω_i, the corresponding vector of unknown parameters is given by $\mathbf{x}(\omega_i)$.For nd ifferent speeds Eq. (33) has the following form

$$\begin{bmatrix} \mathbf{A}(\omega_1) & 0 & 0 & 0 \\ 0 & \mathbf{A}(\omega_2) & 0 & 0 \\ \vdots & \vdots & \vdots & \vdots \\ 0 & 0 & 0 & \mathbf{A}(\omega_n) \end{bmatrix} \begin{Bmatrix} \mathbf{x}(\omega_1) \\ \mathbf{x}(\omega_2) \\ \vdots \\ \mathbf{x}(\omega_n) \end{Bmatrix} = \begin{Bmatrix} \mathbf{b}(\omega_1) \\ \mathbf{b}(\omega_2) \\ \vdots \\ \mathbf{b}(\omega_n) \end{Bmatrix}. \tag{34}$$

The inputs to Eqs. (33) and (34) are the real and imaginary parts of complex displacements at measurement locations on rotors ($\bar{\mathbf{u}}_h^{\mathrm{re}}$, $\bar{\mathbf{u}}_h^{\mathrm{im}}$) and complex currents at AMB locations ($\bar{\mathbf{i}}^{\mathrm{re}}$, $\bar{\mathbf{i}}^{\mathrm{im}}$) obtained from the amplitude and phase of harmonics in full spectrum FFT plots.

$$\bar{\mathbf{u}}_h = \bar{\mathbf{u}}_h^{\mathrm{re}} + \mathrm{j}\bar{\mathbf{u}}_{\mathrm{h}}^{\mathrm{im}}, \qquad \bar{\mathbf{i}} = \bar{\mathbf{i}}^{\mathrm{re}} + \mathrm{j}\bar{\mathbf{i}}^{\mathrm{im}}. \tag{35}$$

A detailed treatment on the theory and application of full spectrum FFT plots is given in [36]. The development of identification algorithm from condensed global EOM has been discussed in this section. The next section discusses the Simulink model used for generating vibration and current outputs.

2.11. Simulink model

The illustrative Simulink$^{\mathrm{TM}}$ model shown in Fig. 5 is built using Eq. (20) and is solved using ODE15s which is a stiff solver. The time domain responses of rotor vibration and control currents in AMB coils in complex form are logged for every $1/2^{16}$ seconds from simulation. The next section discusses the coupled rotor system used for numerical simulation.

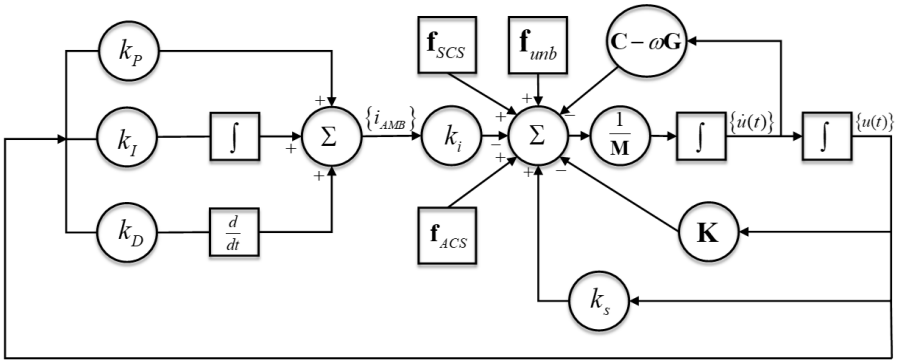

Fig. 5. Representative SIMULINK model of turbine generator supported on TPJBs and AMBs

3. Rotor-bearing-coupling considered for simulation

A coupled rotor system with multiple discs running at 3000 rpm is considered for numerical simulation and is shown in Fig. 6. Rotor-1 and rotor-2 each carry two rigid discs and are supported on AMBs at outboard locations and TPJBs at inboard locations. An intermediate coupling transmits the drive from rotor-1 to rotor-2. The properties of motor and drive end coupling are not included in the model. The properties of rotor, discs, AMB constants and the dimensions of TPJB-1 and TPJB-2 each with 4 pads are given in Table 1. The speed-dependent bearing input properties, i.e., stiffness and damping coefficients at 6 different speeds (500 rpm, 1000 rpm, 1500 rpm, 2000 rpm, 2500 rpm and 3000 rpm) are generated from DyRoBeS© BePerf computer program (Fig. 7a, Fig. 7b). The assumed values of speed-dependent ACS coefficients and AMB coefficients are shown in Fig. 7c and Fig. 7d.

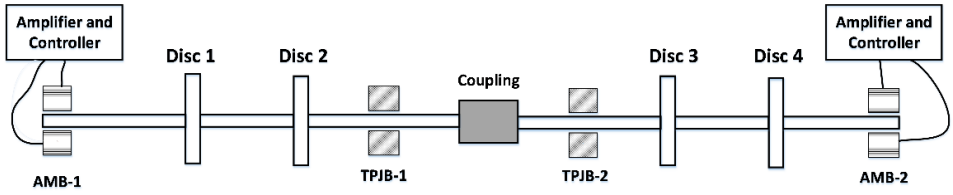

Fig. 6. Coupled rotor system supported on TPJBs and AMBs

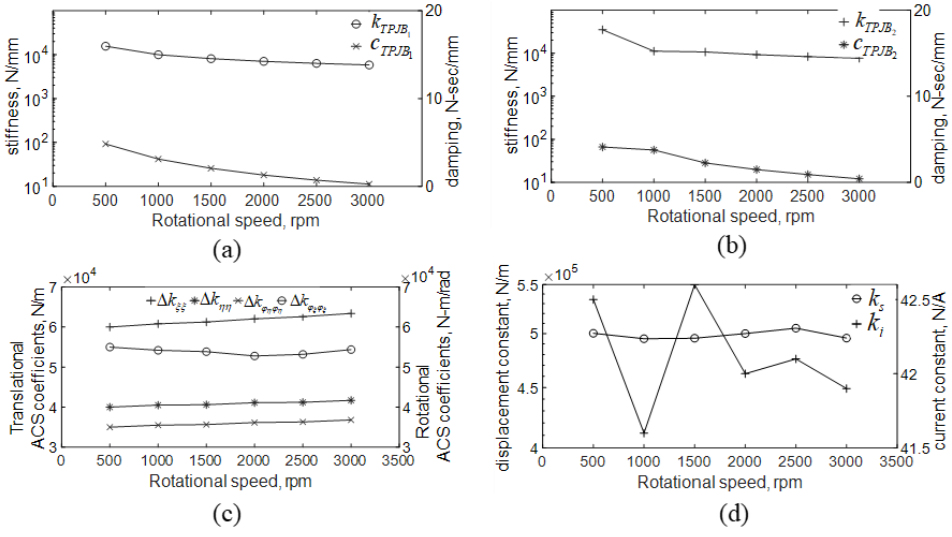

Fig. 7. Speed-dependent inputs: (a) stiffness and damping of TPJB-1 generated from DyRoBes BePerf, (b) stiffness and damping of TPJB-2 generated from DyRoBes BePerf, (c) assumed ACS coefficients, (d) assumed AMB coefficients

Table 1. Specifications of rotor, AMB & TPJBs

Disc				
Mass, kg	Moment of inertia, kg m^2		Unbalance	
			Amplitude, kg m	Phase, rad
$m_{d_1} = 2.25$	$I_{d_1} = 0.0024$	$I_{p_1} = 0.0048$	$e_1 = 4 \times 10^{-5}$	$\beta_1 = \pi/10$
$m_{d_2} = 1.75$	$I_{d_2} = 0.0035$	$I_{p_2} = 0.007$	$e_2 = 3 \times 10^{-5}$	$\beta_2 = \pi/4$
$m_{d_3} = 2.5$	$I_{d_3} = 0.0045$	$I_{p_3} = 0.009$	$e_3 = 4 \times 10^{-5}$	$\beta_3 = \pi/15$
$m_{d_4} = 1.6$	$I_{d_4} = 0.004$	$I_{p_4} = 0.008$	$e_4 = 3 \times 10^{-5}$	$\beta_4 = \pi/12$

Shaft				AMB		
d, m	l_e, m	a_0	a_1	k_p	12 200	A/m
0.17	0.25	0.154	1e-5	k_i	2000	A/(m s)
				k_d	3	(A s)/m

Tilting-pad journal bearing		
Parameter	TPJB-1	TPJB-2
Length (mm)	14	20
Diameter (mm)	20	20
Clearance (μm)	100	100
No. of pads	4	4
Arc length (degree)	72	72
Pivot offset	0.5	0.5
Configuration	*lbp*	*lbp*

4. Results and discussion

The current orbits of AMB-1 and AMB-2 are plotted and shown in Fig. 8. The elliptical nature of orbits is similar to the elliptical displacement orbits in the experimental results reported in [25], which is indicative of the presence of misalignment. Fig. 9 shows full spectrum amplitude and phase plots of the AMB-1 and AMB-2 complex currents. The integer harmonics from −5 to +5 through 0 can be seen.

This is qualitatively similar to the FFT plots obtained from experimental data reported in [25]. This shows the suitability of the steering function $s(t)$ chosen for simulation.

The translational vibration data of rotor at two TPJBs, two AMBs, four discs and two coupling locations and the current data at the two AMBs is acquired from the Simulink model.

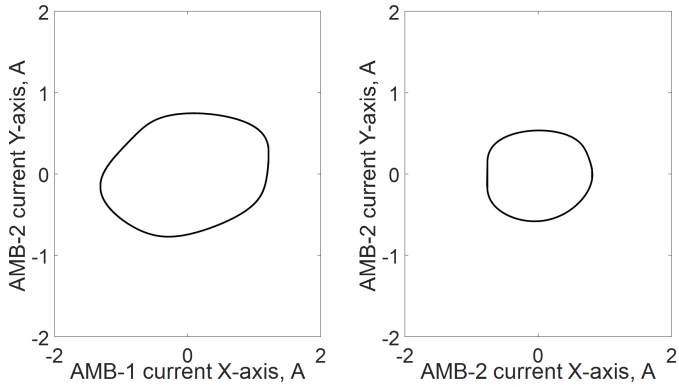

Fig. 8. Complex current orbit of AMB-1 and AMB-2

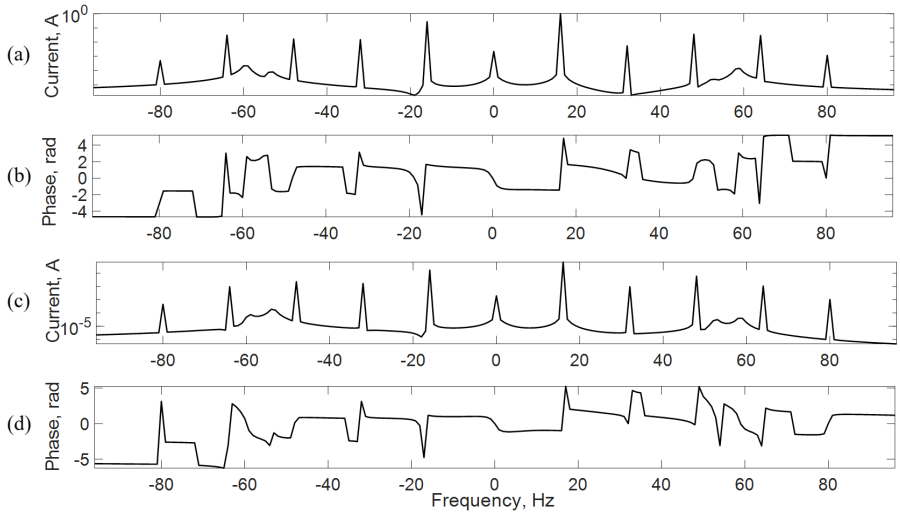

Fig. 9. Full spectrum fft of AMB1: (a) current amplitude, (b) current phase; AMB2: (c) current amplitude, (d) current phase

These are processed through full spectrum FFT algorithm to obtain the amplitude and phase at all positive and negative integer harmonics of interest. The real and imaginary parts of harmonics are then calculated and passed to the identification algorithm.

At each of the six speeds (500 rpm, 1000 rpm, 1500 rpm, 2000 rpm, 2500 rpm, 3000 rpm) a total of 20 parameters comprising 8 unbalance parameters $e_1 \cos\beta_1$, $e_2 \cos\beta_2$, $e_3 \cos\beta_3$, $e_4 \cos\beta_4$, $e_1 \sin\beta_1$, $e_2 \sin\beta_2$, $e_3 \sin\beta_3$, $e_4 \sin\beta_4$, 4TPJB parameters (k_{TPJB_1}, c_{TPJB_1}, k_{TPJB_2}, c_{TPJB_2}), 2 AMB parameters (k_s, k_i) and 6 coupling parameters (k_{rad}, k_{ang}, $\Delta k_{\xi\xi}$, $\Delta k_{\eta\eta}$, $\Delta k_{\varphi_\xi\varphi_\xi}$, $\Delta k_{\varphi_\eta\varphi_\eta}$) are estimated using linear least-squares problem from Eq. (33). The case of 0% noise is studied first. Fig. 10a shows that the error in unbalance estimates is less than 3% with $e_3 \sin\beta_3$ showing

the highest deviation 2.8% at 3000 rpm. Among the TPJB parameters (Fig. 10b) c_{TPJB_1} shows the highest deviation (2%) at 1500 rpm. Among coupling parameters (Fig. 10c), the maximum error is displayed by k_{ang} (−7%) at 2000 rpm. This is the result of hybrid condensation, wherein the angular displacements of coupling are made as the slave DOF. Among AMB parameters, k_s shows a highest deviation of 6.5% at 3000 rpm (Fig. 10d). From Fig. 10c the highest error % in any ACS parameter is around 5%.

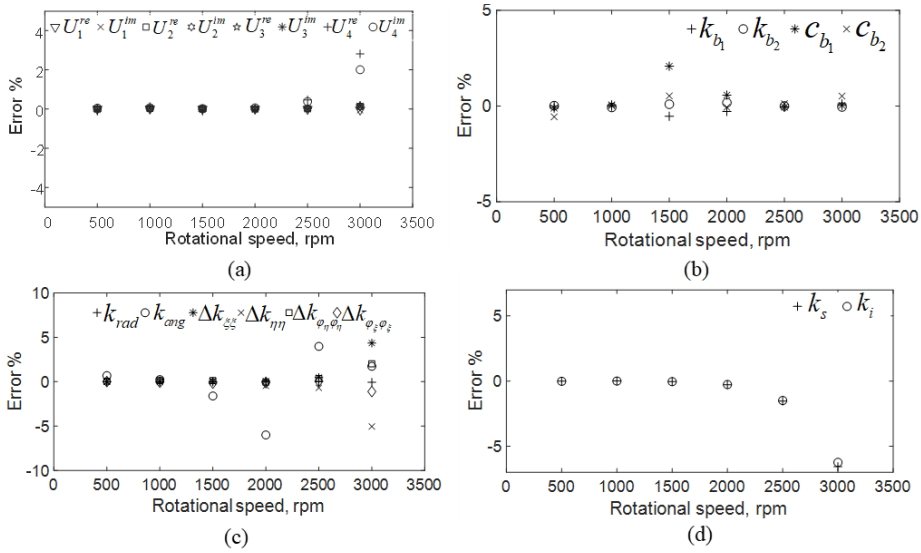

Fig. 10. Error in the estimates with 0% measurement noise: (a) unbalance of discs, (b) speed-dependent TPJB parameters, (c) speed-dependent coupling parameters, (d) speed-dependent AMB parameters

Generally, to model random and interval uncertainties in numerical formulations probabilistic, interval-based approaches are used. In the current work, a measurement error and bias error are introduced to study the sensitivity of identification algorithm. A random Gaussian noise of 5% is added to the vibration and current signals and the estimation is performed again. From Fig. 11a, it is seen that all the unbalance parameters show large deviation at all speeds with $e_2 \cos\beta_2$ varying the highest (10% at 500 rpm). Likewise the errors in TPJB coefficients (Fig. 11b), coupling stiffness parameters (Fig. 11c) and AMB parameters (Fig. 11d) due to 5% measurement noise are c_{TPJB_2} (4.5%) at 1500 rpm, k_{ang} (15%) at 1500 rpm, $\Delta k_{\xi\xi}$ (15%) at 3000 rpm and k_s (14.2%) at 3000 rpm, respectively.

Next, the sensitivity of algorithm to modelling bias is examined. A 5% bias in m_{d_1}, m_{d_2}, m_{d_3}, m_{d_4} and δx_c, δx_{c+1}, $\delta\varphi_{y_c}$, $\varphi_{y_{c+1}}$ is introduced. The maximum errors observed in various parameters are $e_3 \sin\beta_3$ (2.5%) at 3000 rpm (Fig. 12a), c_{TPJB_1} (1.5%) at 1500 rpm (Fig. 12b), k_{ang} (−8%) at 2000 rpm (Fig. 12c), k_s (−6%) at 3000 rpm (Fig. 12d), respectively. The algorithm has shown more sensitivity to

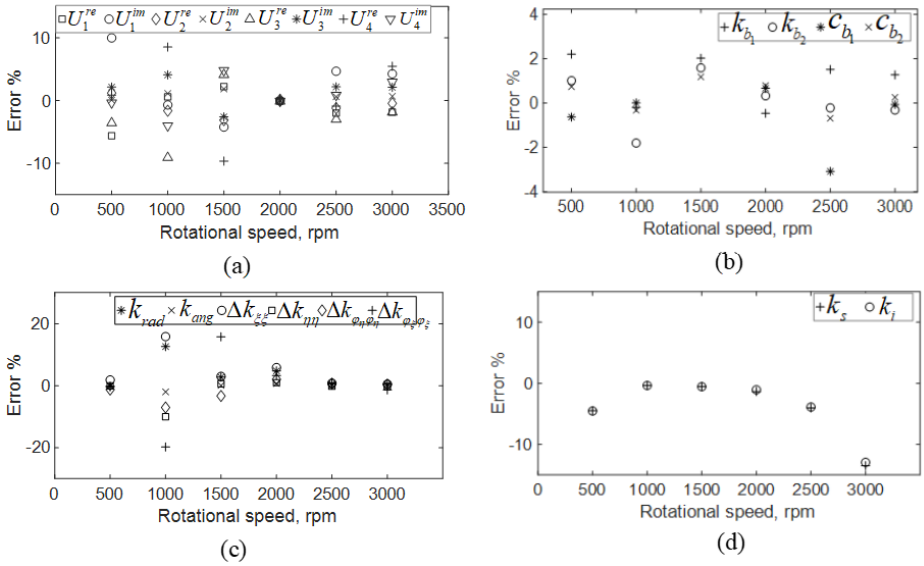

Fig. 11. Error in the estimates with 5% measurement noise: (a) unbalance of discs, (b) speed-dependent bearing parameters, (c) speed-dependent coupling parameters, (d) speed-dependent AMB parameters

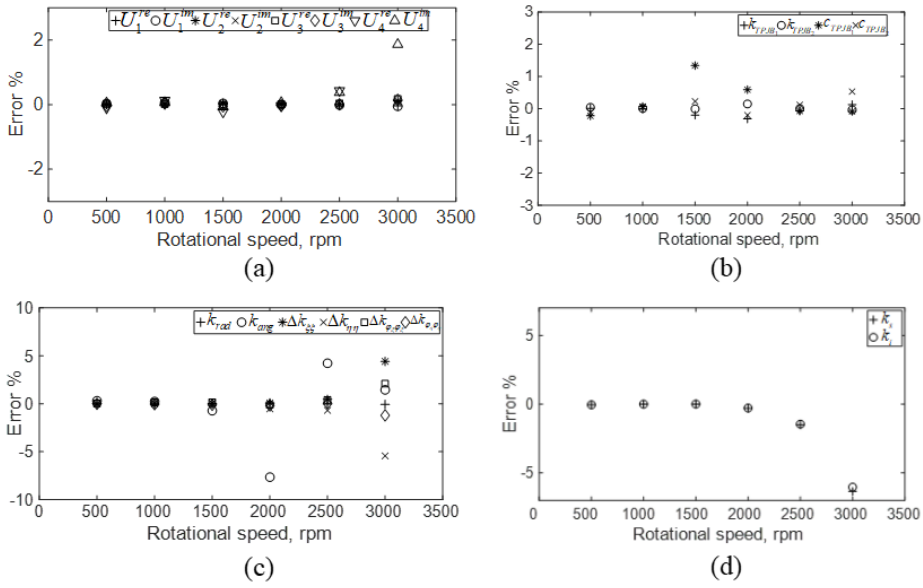

Fig. 12. Error in the estimates with 5% modelling bias (a) unbalance of discs, (b) speed-dependent bearing parameters, (c) speed-dependent coupling parameters, (d) speed-dependent AMB parameters

measurement noise than to bias in parameters. Nevertheless, the error in estimated parameters is within reasonable limits. The absolute values of estimated versus assumed parameters at 3000 rpm for the case of 5% measurement noise are shown in Table 2. It can be seen that the maximum percentage error for ACS parameter $\Delta k_{\xi\xi}$ which denotes parallel misalignment is 15.7%.

Table 2. Assumed values vs estimated values at 3000 rpm for 5% measurement noise

Parameter (units)	Assumed value	Estimated value	Error (%)
U_1^{re}, kg m	1.33E-04	1.31E-04	−1.85
U_2^{re}, kg m	8.49E-05	8.85E-05	4.27
U_3^{re}, kg m	1.17E-04	1.17E-04	−0.44
U_4^{re}, kg m	1.55E-04	1.56E-04	0.68
U_1^{im}, kg m	4.33E-05	4.25E-05	−1.86
U_2^{im}, kg m	8.49E-05	8.66E-05	2.11
U_3^{im}, kg m	2.49E-05	2.63E-05	5.47
U_4^{im}, kg m	4.14E-05	4.26E-05	2.96
k_{TPJB_1}, N/m	5830000	5903738	1.26
k_{TPJB_2}, N/m	7660000	7635603	−0.32
c_{TPJB_1}, N s/m	11200	11192	−0.07
c_{TPJB_2}, N s/m	12100	12131	0.25
k_s, N/m	495600	428749	−13.49
k_i, N/A	41.9	36	−12.95
k_{rad}, N/m	225000	224243	−0.34
k_{ang}, N m/rad	200000	160492	−19.75
$\Delta k_{\xi\xi}$, N/m	63400	73409	15.79
$\Delta k_{\eta\eta}$, N/m	41700	43081	3.31
$\Delta k_{\varphi_\xi\varphi_\xi}$, N m/rad	36800	37155	0.97
$\Delta k_{\varphi_\eta\varphi_\eta}$, N m/rad	54380	53653	−1.34

In this section, numerical results from simulation and results of inverse problem are presented. Even in the presence of 5% measurement noise, the maximum error in the estimation of ACS parameters which is representative of misalignment is found to be less than 15%. This shows the robustness of the identification algorithm. The next section discusses as to how the ideas presented so far can be used to detect the presence of parallel and angular misalignments in real rotors.

5. Method of application in real rotors

Fig. 13 is the pictorial representation of how the algorithm can be used for condition monitoring of misalignment in real rotors.

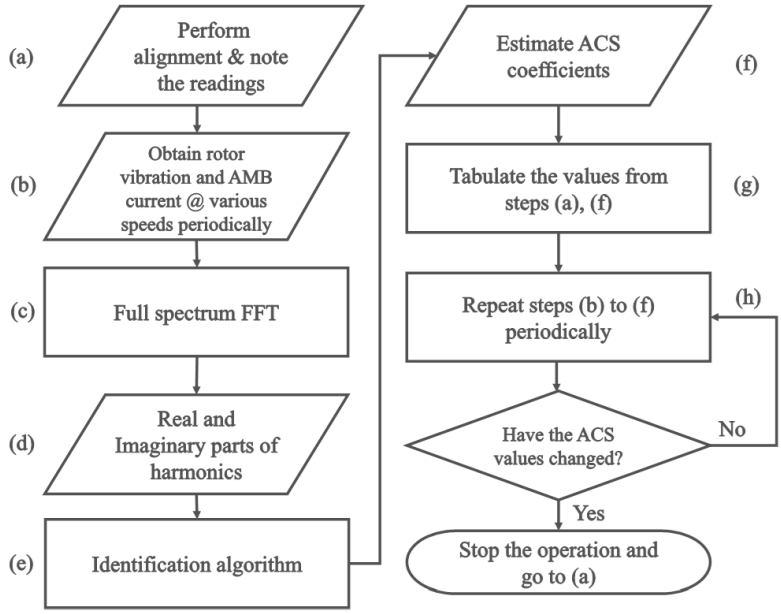

Fig. 13. Method of application of identification algorithm in real rotors

6. Conclusions

The objective of the present work is the modelling of misaligned coupling using the SCS and ACS matrices and identification of ACS coefficients at various speeds in coupled rotors

1. The intermediate coupling stiffness has two components: SCS and ACS matrices. Parallel and angular misalignments have been represented by ACS coefficients in the corresponding directions.
2. The mathematical model of coupling is developed based on weight dominance criteria and the selection of suitable steering function.
3. The global EOM is assembled and condensed by grouping the coupling rotational DOF, which are difficult to measure experimentally, as slave DOF. An inverse problem is developed from frequency domain representation of the condensed EOM.
4. The inputs to the algorithm are obtained from the full spectrum plots of vibration at rotor master nodes and currents at AMB nodes. The solution to the inverse problem is sought at six different speeds thereby yielding

the speed-dependent unknown system parameters. The estimated values in the presence of noise and modelling bias showed acceptable level of error thereby validating the robustness of identification algorithm.

5. The novelty of the present work is the development of methodology that has potential for the condition monitoring of misalignment in real rotors.
6. The current numerical work shall be experimentally validated in future to demonstrate the effectiveness of identification algorithm for condition monitoring using AMBs. The experimental results can then be compared with those of traditional condition monitoring techniques.
7. This method primarily differs from the other condition monitoring methods in the manner characterization of misalignment is made. This method quantifies the amplitudes and phase of harmonics of vibration and current that arise due to misalignment using AMB that also acts as support bearing for the rotor system.

Acknowledgement

The author would like to thank K Ramesh, GM(AERDC) for granting permission to publish this work.

References

[1] R. Siva Srinivas, R. Tiwari, and Ch. Kannababu. Application of active magnetic bearings in flexible rotordynamic systems – A state-of-the-art review. *Mechanical Systems and Signal Processing*, 106:537–572. 2018. doi: 10.1016/j.ymssp.2018.01.010.

[2] B. Sankar, A.S. Sekhar, and S. Jana. Estimation of magnetic bearing constant in active magnetic bearings. *Mechanical Systems and Signal Processing*, 198:110411, 2023. doi: 10.1016/j.ymssp.2023.110411.

[3] H.A.P. Silva and R. Nicoletti. Rotor vibration control using tilting-pad journal bearing with active pads – Numerical and experimental results. *Journal of Sound and Vibration*, 546:117441, 2023. doi: 10.1016/j.jsv.2022.117441.

[4] J.H. Ye, D. Shi, Y.S. Qi, J.H. Gao, and J.X. Shen. Vibration suppression for active magnetic bearings using adaptive filter with iterative search algorithm. *Transactions on Electrical Machines and Systems*, 8(1):61–71, 2024. doi: 10.30941/CESTEMS.2024.00007.

[5] F. Xiong, Y. Li, and J-Ch. Han. Method and experimental study of axial vibration suppression of propulsion shaft system supported by hybrid magnetic bearings. *Ocean Engineering*, 313(2):119413, 2024. doi: 10.1016/j.oceaneng.2024.119413.

[6] G. Majumder and R. Tiwari. Application of active magnetic bearings in control and estimation of geared-rotor faults in high speed offset spur gear transmission system. *Mechanical Systems and Signal Processing*, 176:109113, 2022. doi: 10.1016/j.ymssp.2022.109113.

[7] G. Majumder and R. Tiwari. Experimental study on vibration control of spur geared rotor system with active magnetic bearings. *Journal of Sound and Vibration*, 532:117005. 2022. doi: 10.1016/j.jsv.2022.117005.

[8] A. Bouaziz, S. Bouaziz, T. Hentati, J.Y. Challey, and M. Haddar. Vibrations monitoring of high speed spindle with active magnetic bearings in presence of defects. *International Journal of Applied Electromagnetics and Mechanics*, 49(2):207–221, 2015. doi: 10.3233/JAE-140190.

[9] M.O.T. Cole, C. Chamroon, and P. Ngamprapasom. Force feedback control for active stabilization of synchronous whirl orbits in rotor systems with nonlinear stiffness elements. *Journal of Vibration and Acoustics*, 134(2):021018, 2012. doi: 10.1115/1.4005021.

[10] B. Xiang, T. Wen, and Z. Liu. Vibration analysis, measurement and balancing of flywheel rotor suspended by active magnetic bearing. *Measurement*, 197:111305, 2022. doi: 10.1016/j.measurement.2022.111305.

[11] R. Tiwari and P. Kumar. An innovative virtual trial misalignment approach for identification of unbalance, sensor and active magnetic bearing misalignment along with its stiffness parameters in a magnetically levitated flexible rotor system. *Mechanical Systems and Signal Processing*, 167(A):108540, 2022. doi: 10.1016/j.ymssp.2021.108540.

[12] B. Nayek, A.S. Das, and J.K. Dutt. Model based estimation of inertial parameters of a rigid rotor having dynamic unbalance on Active Magnetic Bearings in presence of noise. *Applied Mathematical Modelling*, 97:701–720, 2021. doi: 10.1016/j.apm.2021.04.015.

[13] A. El-Shafei and A.S. Dimitri. Controlling journal bearing instability using active magnetic bearings. *Journal of Engineering for Gas Turbines and Power*,132(1):012502, 2010. doi: 10.1115/1.3078785.

[14] B. Riemann, E.A. Perini, K. Lucchesi Cavalca, H.F. de Castro, and S. Rinderknecht. Oil whip Instability control using μ-synthesis technique on a magnetic actuator. *Journal of Sound and Vibration*, 332(4):654–673, 2013. doi: 10.1016/j.jsv.2012.09.034.

[15] A.H. Pesch and J.T. Sawicki. Stabilizing hydrodynamic bearing oil whip with μ-synthesis control of an active magnetic bearing. In: *Proceedings of ASME Turbo Expo 2015: Turbine Technical Conference and Exposition. Volume 7A: Structures and Dynamics*, Montréal, Canada, 15–19 June 2015, pp. V07AT31A029. doi: 10.1115/GT2015-44059.

[16] A.S. Dimitri, J. Mahfoud, and A. El-Shafei. Oil whip elimination using fuzzy logic controller. *Journal of Engineering for Gas Turbines and Power*, 138(6):062502, 2016. doi: 10.1115/1.4031759.

[17] G. Mani, D.D. Quinn, and M. Kasarda. Active health monitoring in a rotating cracked shaft using active magnetic bearings as force actuators. *Journal of Sound and Vibration*, 294(3):454–465, 2006. doi: 10.1016/j.jsv.2005.11.020.

[18] J.T. Sawicki, D.L. Storozhev, and J.D. Lekki. Exploration of NDE properties of AMB supported rotors for structural damage detection. *Journal of Engineering for Gas Turbines and Power*, 133(10):102501, 2011. doi: 10.1115/1.4002908.

[19] Z.S. Spakovszky, J.D. Paduano, R. Larsonneur, A. Traxier, and M.M. Broght. Tip clearance actuation with magnetic bearings for high-speed compressor stall control. *Journal of Turbomachinery*, 123(3):464–472, 2001. doi: 10.1115/1.1370163.

[20] S.Y. Yoon, Z. Lin, W. Jiang, and P.E. Allaire. Flow-rate observers in the suppression of compressor surge using active magnetic bearings. In: *Proceedings of the ASME Turbo Expo 2012: Turbine Technical Conference and Exposition. Volume 8: Turbomachinery*, pages 2775–2784, Copenhagen, Denmark, June 11–15, 2012. doi: 10.1115/GT2012-70011.

[21] H.P. Viveros and R. Nicoletti. Lateral vibration attenuation of shafts supported by tilting-pad journal bearing with embedded electromagnetic actuators. *Journal of Engineering for Gas Turbines and Power*, 136(4):042503, 2014. doi: 10.1115/1.4026038.

[22] Pilotto R, Nordmann R et al. (2017) Use of magnetic bearings in vibration control of a steam turbine with oil film bearings. In: *24th International Congress on Sound and Vibration*, pages 534-541, London, UK, 23–27 July, 2017.

[23] N. Sarmah and R. Tiwari. Numerical and experimental study on quantitative assessment of multiple fault parameters in a warped internally damped rotor with a transverse fatigue crack integrated with an active magnetic bearing. *Mechanical Systems and Signal Processing*, 174:109112, 2022. doi: 10.1016/j.ymssp.2022.109112.

[24] P. Zhang and C. Zhu C. Vibration control of base-excited rotors supported by active magnetic bearing using a model-based compensation method. *IEEE Transactions on Industrial Electronics*, 71(1):261–270, 2024. doi: 10.1109/TIE.2023.3243263.

[25] T.H. Patel and A.K. Darpe. Experimental investigations on vibration response of misaligned rotors. *Mechanical Systems and Signal Processing*, 23(7):2236–2252, 2009. doi: 10.1016/j.ymssp.2009.04.004.

[26] A.W. Lees. Misalignment in rigidly coupled rotors. *Journal of Sound and Vibration*, 305(1-2):261–271, 2007. doi: 10.1016/j.jsv.2007.04.008.

[27] M. Lal and R. Tiwari. Multiple fault identification in simple rotor-bearing-coupling systems based on forced response measurements. *Mechanism and Machine Theory*, 51:87–109, 2012. doi: 10.1016/j.mechmachtheory.2012.01.001.

[28] Y. Su, Y. Gu, P.S. Keogh, S. Yu, and G. Ren. Nonlinear dynamic simulation and parametric analysis of a rotor-AMB-TDB system experiencing strong base shock excitations. *Mechanism and Machine Theory*, 155:104071, 2021. doi: 10.1016/j.mechmachtheory.2020.104071.

[29] S. Bouaziz, N.B. Messaoud, M> Maatar, T. Fakhfakh, and M. Haddar. A theoretical model for analyzing the dynamic behavior of a misaligned rotor with active magnetic bearings. *Mechatronics*, 21(6):899–907, 2011. doi: 10.1016/j.mechatronics.2011.05.001.

[30] S. Bouaziz, N.B. Messaoud,J.Y. Cholley, M. Maatar, and M. Haddar. Transient response of a rotor-AMBs system connected by a flexible mechanical coupling. *Mechatronics*, 23(6):573–580, 2013. doi: 10.1016/j.mechatronics.2013.05.002.

[31] T. Soni, J.K. Dutt, and A.S. Das. Magnetic bearings for marine rotor systems – effect of standard ship maneuver. *IEEE Transactions on Industrial Electronics*, 68(2):1055–1064, 2021. doi: 10.1109/TIE.2020.2967664.

[32] S.K. Kuppa and M. Lal. Dynamic behaviour analysis of coupled rotor active magnetic bearing system in the supercritical frequency range. *Mechanism and Machine Theory*, 152:103915, 2020. doi: 10.1016/j.mechmachtheory.2020.103915.

[33] W.J. Chen. A note on computational rotor dynamics. *Journal of Vibration and Acoustics*, 120(1):228–233, 1998. doi: 10.1115/1.2893810.

[34] W.J. Chen and E.J. Gunter. *Introduction to Dynamics of Rotor Bearing Systems*. Trafford Publications, 2007.

[35] G. Schweitzer and E.H.Maslen (eds). *Magnetic Bearings: Theory, Design and Application to Rotating Machinery*. Springer-Verlag, 2009. doi: 10.1007/978-3-642-00497-1.

[36] R. Tiwari. *Rotor Systems: Analysis and Identification*. CRC Press, 2017. doi: 10.1201/9781315230962.

[37] C. Shravankumar and R. Tiwari. Identification of stiffness and periodic breathing forces of a transverse switching crack in a Laval rotor. *Fatigue and Fracture of Engineering Materials and Structures*, 36(3):254–269, 2012. doi: 10.1111/j.1460-2695.2012.01718.x.

[38] M.I. Friswell, J.E.T. Penny, S.D. Garvey, and A.W. Lees. *Dynamics of Rotating Machines*. Cambridge University Press, 2010. doi: 10.1017/CBO 9780511780509.